ADVANCED FUNCTIONAL MATERIALS
www.afm-journal.de

Graphene as an Electron Shuttle for Silver Deoxidation: Removing a Key Barrier to Plasmonics and Metamaterials for SERS in the Visible

Maria Losurdo, Iris Bergmair, Babak Dastmalchi, Tong-Ho Kim, Maria M. Giangregroio, Wenyuan Jiao, Giuseppe V. Bianco, April S. Brown, Kurt Hingerl, and Giovanni Bruno*

The role of graphene in enabling deoxidation of silver nanostructures, thereby contributing to enhance plasmonic properties and to improve the temporal stability of graphene/silver hybrids for both general plasmonic and metamaterials applications, as well as for surface enhanced Raman scattering (SERS) substrates, is demonstrated. The chemical mechanism occurring at the graphene–silver oxide interface is based on the reduction of silver oxide triggered by graphene that acts as a shuttle of electrons and as a kind of catalyst in the deoxidation. A mechanism is formulated, combining elements of electron transfer, role of defects in graphene, and electrochemical potentials of graphene, silver, and oxygen. Therefore, the formulated model represents a step forward from the simple view of graphene as barrier to oxygen diffusion proposed so far in literature. Single layer graphene grown by chemical vapor deposition is transferred onto silver thin films, a periodic silver fishnet structure fabricated by nanoimprint lithography, and onto silver nanoparticle ensembles supporting a localized surface plasmon resonance in the visible range. Through the study of these nanostructured graphene/Ag hybrids, the effectiveness of graphene in preventing and reducing oxidation of silver plasmonic structures, keeping silver in a metallic state over months at air exposure, is demonstrated. The enhanced and stable plasmonic properties of the silver-fishnet/graphene hybrids are evaluated through their SERS response for detecting benzyl mercaptane.

1. Introduction

One of the most fascinating current research fields is aimed at controlling and manipulating light at the nanoscale—a key objective of the emerging discipline of plasmonics[1]—through the exploitation and tailoring of the localized surface plasmon resonance (LSPR), a collective oscillation of conduction electrons that becomes resonant when noble metal nanostructures are irradiated by appropriate light of the right frequency.[2] New materials and new processes applied to conventional materials can provide new functionalities and potential to plasmonics. From this perspective, we address the following question: what is the potential of combining the attractive materials characteristics of graphene and silver nanostructures for plasmonic- and meta-materials?

Graphene with its superior mechanical, thermal, chemical and electrical properties[3] is emerging as a versatile material with applications in electronics,[4] sensing, catalysis,[5] batteries,[6] photovoltaic[7] industries, and more recently in plasmonics.[8] The use of nanoscale objects limits the length scale for all noble-metal plasmonic devices to the nanometre scale, whereas it has been recently reported[9] that the surface plasmon resonance in graphene can be locally enhanced at the sub-nanometer scale by the presence of single point defects, representing a length scale smaller than $\lambda/200$. This suggests that doped monolayer graphene could be used in the development of atomic-scale nanoplasmonics and quantum plasmonic devices.[10] Very recent work has proposed that plasmon polaritons—coupled excitations of photons and charge carriers—in graphene are a promising way to achieve the electronic control of light.[8] The tuning of the plasmon spectrum is possible through electrical or chemical modifications of the charge carrier density.[11]

Dr. M. Losurdo, Dr. M. M. Giangregorio,
Dr. G. V. Bianco, Prof. G. Bruno
Institute of Inorganic Methodologies and of Plasmas-CNR
Via Orabona, 4, 70126, Bari, Italy
E-mail: maria.losurdo@cnr.it
Dr. I. Bergmair
Functional Surfaces and Nanostructures
PROFACTOR GmbH, Im Stadtgut A2, 4407, Steyr-Gleink, Austria
Dr. B. Dastmalchi, Prof. K. Hingerl
Center for Surface- and Nanoanalytics
Johannes Kepler University Linz
Altenbergerstr. 69, 4040, Linz, Austria
Dr. T. H. Kim, Dr. W. Jiao, Prof. A. S. Brown
Electrical and Computer Engineering Department
Duke University
Durham, 27709, NC, USA

DOI: 10.1002/adfm.201303135

On the other hand, silver (Ag) is an excellent plasmonic material for the visible range.[12] Silver nanoparticles (Ag NPs) and nanostructures with tunable LSPR from the visible to the NIR have been found to be useful in various applications, especially for surface enhanced Raman scattering (SERS).[13] This is because Ag NPs have an optical efficiency, defined by the ratio of the scattering cross section to the extinction cross-section, larger than the gold nanoparticles of the same diameter in a broad spectral range (e.g., 400–1400 nm).[14]

Silver is also considered an important material for metamaterials for achieving negative refractive index in the visible due to its significantly lower losses as compared to gold at visible frequencies.[15] Although Ag is classified as a noble plasmonic metal, its primary drawback is its chemical instability leading to silver oxidation that red-shifts and dampens optical resonances.[16] Therefore, in order to exploit Ag nanostructures in plasmonic structures, as well as for achieving stable Ag-based metamaterials in the visible, there is still a crucial need to develop new protection layers for Ag nanostructures, which are ultrathin, gas-impermeable, conductive, and enable long-term stability without the loss of optical properties required for practical photonic and plasmonic devices.

In this context, the chemistry of the oxygen-silver interaction is still of considerable fundamental and technological relevance. At 300 K and atmospheric pressure, O_2 dissociatively chemisorbs (O_{ads}) on silver surfaces, where it reacts to form silver oxides according to the reactions (thermal energies are of the order of 25 kJ mol^{-1}, so both processes can occur at RT):[17]

$$\mathrm{Ag} + \mathrm{O_{ads}} \rightarrow \mathrm{AgO} \quad (\Delta H^\circ = -24.3\ \mathrm{kJ\ mol^{-1}};\ \Delta G^\circ = -27.6\ \mathrm{kJ\ mol^{-1}}) \tag{1}$$

$$2\ \mathrm{Ag} + \mathrm{O_{ads}} \rightarrow \mathrm{Ag_2O} \quad (\Delta H^\circ = -31.1\ \mathrm{kJ\ mol^{-1}};\ \Delta G^\circ = -11.2\ \mathrm{kJ\ mol^{-1}}) \tag{2}$$

The formation of Ag oxides can be seen in changes of the optical properties of Ag, which are fundamentally described by its complex dielectric function $\varepsilon = \varepsilon_1 + i\varepsilon_2$ that represents the internal response of a material to the electric field of incident light. The transition from metallic Ag to an oxide reduces the free electron density and, hence, decreases the imaginary part of the pseudodielectric function, $<\varepsilon_2>$, and increases the real part of the pseudodielectric function, $<\varepsilon_1>$, causing a red-shift and a damping of plasmonic bands (see also an example in the discussion below).[18] This also has detrimental consequences on the functional properties of plasmonic Ag nanostructures, such as a decrease of the enhancement factor in SERS.[19]

Despite the fact that graphene is prone to oxidation, due to its local curvature (e.g., ripples),[20] the pioneering work of Ruoff and co-workers[21] showed that CVD graphene grown on copper and nickel effectively suppresses metal oxidation by posing a high energy barrier to diffusion of oxygen. In this previous work, graphene was CVD grown on the same metal (copper), and although CVD graphene is polycrystalline and characterized by grain boundaries,[22] over short times scales the bonding at the interface as well as electrostatic interactions between the as-grown graphene and the Ni and Cu are expected to passivate the defects, i.e., grain boundaries and dangling bonds at the metal interface, and to prevent metal oxidation. On the other hand, when graphene is transferred to another metal or it is sandwiched between two different metals, graphene may break and so there could parts of the sample which are not covered by graphene, decreasing the effectiveness of graphene as "barrier" to oxygen. Therefore, considering the challenging of preserving the integrity of graphene during the transfer process to another structured substrate, it is interesting to explore how the electronic properties of the graphene/metal hybrid change and contribute to oxidation/reduction reactions of either graphene or silver. The interaction between Ag and graphene and the resulting changes in the graphene electronic structure were theoretically investigated by Giovannetti et al.[23] Experimentally, graphene oxide/silver composites have been primarily synthesized so far by depositing Ag NPs on graphene-oxide or by their simultaneous reduction in solutions of Ag salts.[24–26] Visible-light-triggered plasmonic photocatalysts based on silver-graphene oxide composites is expected to display excellent plasmonic photocatalytic performance useful for the degradation of pollutants under visible- light irradiation. Recently, Ag NPs were evaporated on exfoliated graphene by Lee at al.[27] inducing n-type doping in the graphene through electron transfer driven by the work function difference.[28] A thin layer of Ag was deposited on chemical vapor deposited (CVD) graphene with the aim of controlling the transport properties of graphene by metal deposition,[29] since metals like Ag and Cu shift the Fermi level of the graphene from the Dirac point into the conduction band. Very recently, graphene has been proposed as an effective solution to the problem of silver sulfidation, by transferring CVD graphene on silver nanoantennas.[30] The same group also demonstrates an increased sensitivity of Ag–graphene nanoantennas as sensors with a much higher resolution. Therefore, the combination of these two materials, graphene and silver, may lead to integration of their properties in new hybrid materials that appear promising for enhancing the performance of numerous applications including plasmonics, catalysis and sensing.

In this work, we study graphene–silver (and/or silver oxide) electron transfer in order to reveal fundamental aspects of the reduction chemistry of silver oxides with the ultimate goal of inhibiting Ag oxidation and enhancing graphene–silver based plasmonics. We have transferred CVD graphene onto an ultrathin silver film, nanoparticles ensemble and to a periodic silver fishnet metamaterial fabricated by nanoimprint lithography.[31] We address two important issues: the influence of graphene and its chemical transformations on the chemical and optical properties of plasmonic silver nanoarrays and, inversely, the influence of plasmonic near-fields generated by the Ag LSPR on the optical properties of graphene. We provide evidence that due to its redox properties, graphene can transfer electrons, and we can take advantage of this electron transfer process to reduce silver oxidation and provide more stable plasmonic- and meta-materials. The effectiveness of the approach and the stability of the graphene/Ag plasmonic platform are proven using surface enhanced Raman scattering (SERS) demonstration for detection of benzyl mercaptane (BZM). A comparison of the SERS spectra of BZM on graphene/Ag NPs and on a graphene/Ag fishnet is also carried out to better understand how to realize an optimal

graphene-Ag-based SPR substrate achieving and maintaining high SERS sensitivity.

2. Results and Discussion

2.1. Evidences for Silver Deoxidation and Electron Transfer from Graphene

Figure 1 shows scanning (SEM) electron micrographs without and with CVD graphene transferred on top of a periodic Ag fishnet, an ultrathin (20 nm) Ag film and on Ag self-assembled nanoparticles (NPs). Graphene transferred on the Ag film shows a well ordered strip pattern, as recently reported by Tian et al.[32] AFM enables characterization of the roughness of the prepared samples; specifically, the polycrystalline Ag film evaporated onto a SiO_2/Si wafer has a surface roughness (root mean square roughness, rms, measured on a 5 μm × 5 μm area) of rms = 2.6 nm, while the graphene transferred to the same SiO_2/Si substrate has a typical rms = 1 nm over a 5 μm × 5 μm area that includes wrinkles and very flat graphene rms = 0.37 nm (on a 1 μm × 1 μm scan not including wrinkles), consistently with previous AFM reports of transferred CVD graphene.[33] When graphene is transferred to an Ag film, the roughness decreases to rms = 2.0 nm indicating a slight smoothing of the Ag film by the graphene. When graphene is transferred to the Ag fishnet, it covers the holes in the structure; furthermore, tilt SEM images (Figures 1c,f) show the effect of pillars in the Ag fishnet and of the Ag nanoparticles topography on the graphene adhesion to those nanostructures, indicating that the graphene may be strained (as discussed in more detail below); the graphene conforms to the top surface of nanoparticles but droops down between the nanoparticles, adhering to the SiO_2 surface.

Figure 2 shows typical Raman spectra acquired at various points across the sample (the example in the figure is for the fishnet but applies similarly to Ag film and to the NPs ensemble). The Raman spectra of graphene on the fishnet and on the continuous Ag film exhibit the characteristic defect-related D feature (1351 cm^{-1}), the G-band corresponding to the vibration of sp2 bonded carbon atoms, and the 2D band (second order of the D band).[30,34] The 2D/G ratio (although it is also affected by doping) indicates that there are regions of monolayer graphene ($I_{2D}/I_G \approx 2$, supported also by the fit of both the G and 2D bands by a single Gaussian peak) and bilayer ($I_{2D}/I_G \approx 1$) graphene resulting from ripples formed during the transfer process and from the morphology of the fishnet and NPs. For our CVD graphene, grains have been identified using the same approach reported elsewhere,[35] and from the image reported in Figure 2a, a grain size distribution in the 40–100 μm^2 range is observed. A line Raman scan along the grains indicated that no D peak is observed in the center of graphene grains, indicating the absence of a significant number of structural defects, while a D peak is observed at graphene grain boundaries. Therefore, the D peak observed in Figure 2 could be ascribed mainly to grain boundaries, although an additional contribution coming from the transfer process cannot be ruled out.

It is well-known that the positions of the G and 2D bands are dependent on doping[34] as well as on strain/stress[36–39] in the

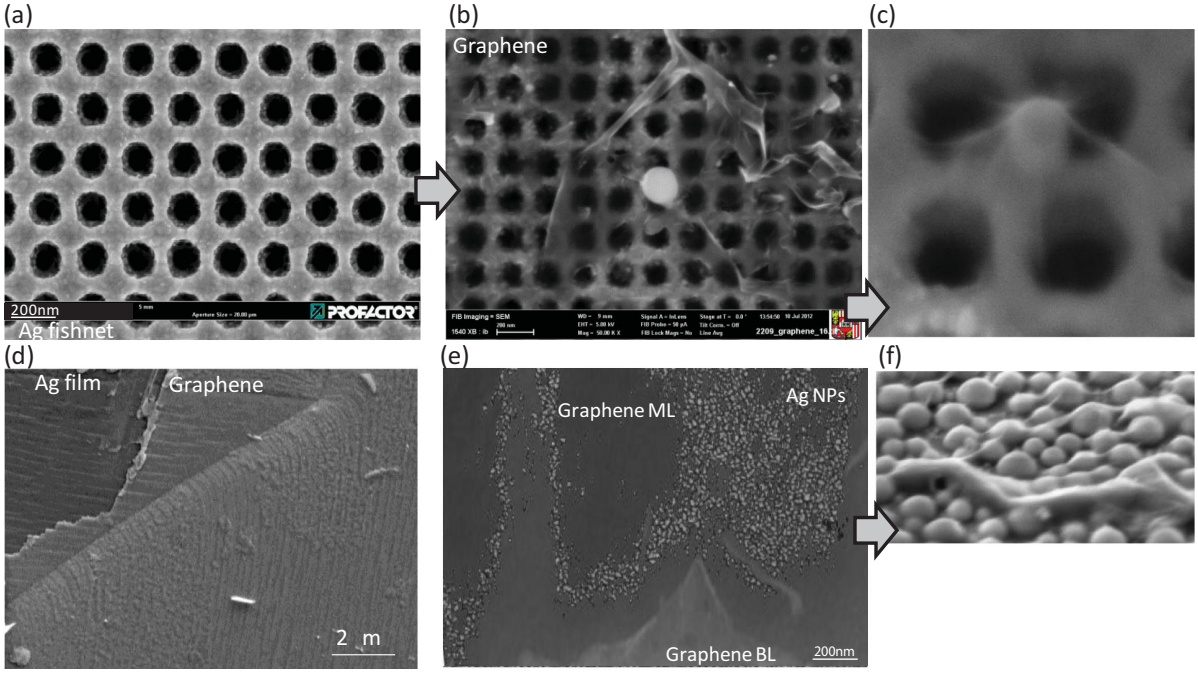

Figure 1. SEM images of: a) a periodic Ag fishnet as fabricated by nanoimprint lithography, b) with graphene transferred on it, and c) a tilted image of an enlarged region to show adhesion of graphene altered by pillars and holes present in the Ag fishnet; d) an ultrathin (20 nm) Ag film with graphene transferred on top; d) self-assembled evaporated Ag NPs with graphene transferred ontop (in the case of Ag NPs/graphene, we intentionally show a region where graphene is not continuous to make clearly visible the Ag NPs underneath); f) a tilted image for the nanoparticles showing the non-conformal adhesion of graphene on them.

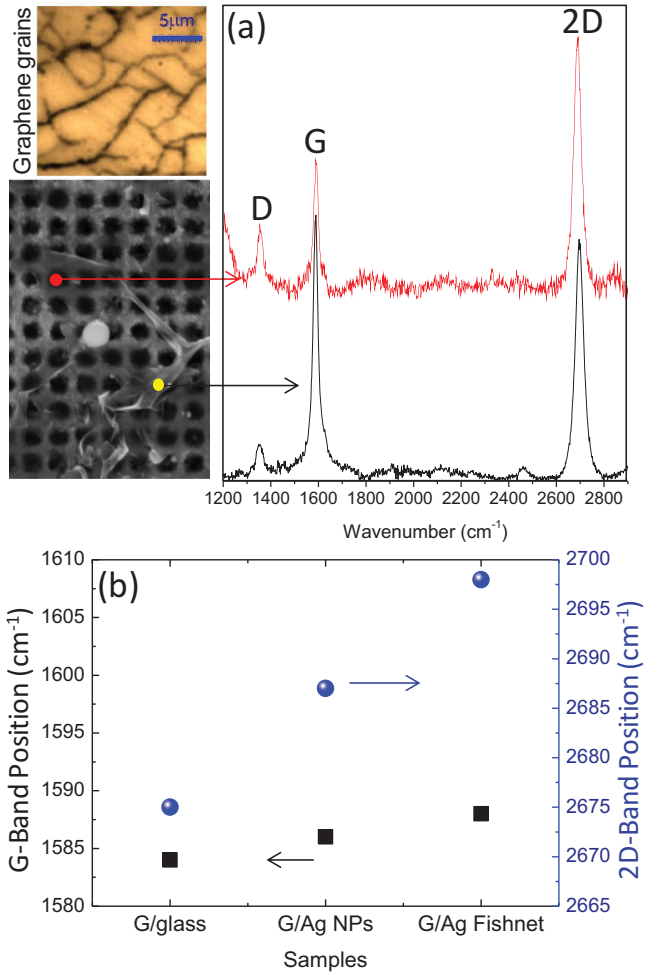

Figure 2. a) Typical Raman spectra acquired (laser 532 nm) in two representative points of the Ag fishnet, indicating regions of graphene monolayer and bilayer as also seen in the images of Figure 1. b) Position of the Raman G- and 2D-bands for the various graphene samples. An optical microscope image of the graphene grains for the as-grown graphene (before transferring to Ag structures) is also shown as top-inset.

structures. Figure 2b provides details on the shift of the Raman G- and 2D-bands from which electronic interactions between the graphene and silver can be inferred. Specifically, for the case of graphene on the silver film and fishnet, it can be observed that the G band shifted approximately ≈4 cm^{-1} from 1585 cm^{-1} (pristine graphene on glass) to 1589 cm^{-1} (Ag doped graphene) and the 2D band shifted approximately ≈20 cm^{-1} from 2675 cm^{-1} (pristine graphene) to 2695 cm^{-1} (Ag –doped graphene). These shifts may be related to both p-type doping of graphene resulting from the transfer of electrons from graphene to silver/silver oxides and to strain as discussed below. Commonly it is observed[34] that the position of the 2D peak changes slowly at low doping level, while the G peak is more sensitive, whereas in this study the 2D band exhibits larger shift in comparison to the G band, especially for the Ag fishnet, indicating that a contribution to the shift from the strain of the graphene resulting from the adhesion to this complex topography is also possible, as shown by the tilt SEM images in Figure 1c,f. Specifically, the 2D peak is blue-shifted by 20 cm^{-1}, while the G peak is blue-shifted only by 4 cm^{-1} and remains a single peak without any splitting. Our observations are very similar to those reported by Wang et al.[40] for graphene transferred to gold and silver. While the G-band shift of approximately 4 cm^{-1} is similar to that observed by other authors resulting from charge transfer from graphene to silver NPs,[41] the blue-shift of the 2D peak is relatively larger than the G peak and indicates that mechanical strain induced by the non conformal covering of graphene to the structured Ag is present.[36,38,39] Thus, it can be seen that, in the case of graphene on structured Ag, the Raman spectrum does not uniquely relate to charge transfer since it also includes a strain component. Therefore, corroborating information about the charge transfer and chemical state of graphene and Ag has been obtained by x-ray photoelectron spectroscopy (XPS). Survey XPS spectra have been acquired to ascertain the presence of the various elements present on the samples. Only carbon, oxygen, and silver have been detected ruling out any contamination from sulfur or chlorine commonly associated with the corrosion of silver.[42] The Ag 3d peaks obtained from the as-prepared Ag samples and for Ag/graphene samples also as a function of oxidation by air exposure are presented in **Figure 3**. Comparison of these peaks reveals some major differences between samples. Specifically, the Ag/SiO_2/Si sample shows fit-components due to Ag, Ag_2O and AgO,[43] indicating a fast surface oxidation soon after deposition; after both a week and a month of air exposure, the only component detected is AgO, indicating the complete oxidation of the Ag silver layer. Interestingly, a different evolution with time of the Ag peak is observed between the samples. Specifically, for the Ag/SiO_2 sample, after a week of air exposure all of the Ag is oxidized to AgO as stated above. Noteworthy, when silver is covered by a graphene monolayer, a significant part of silver remains metallic even after one month of air exposure. A fraction of silver oxide and unpassivated silver is still present when a monolayer of graphene is transferred due to features such as holes, cracks and micron-size defects present in the graphene monolayer; however, the deoxidation and oxidation resistance is almost total when a bilayer graphene is used instead by inhibiting the permeation of oxygen through the defects holes present in the graphene. There is clearly a compromise concerning the graphene thickness that has to be applied considering the need to realize full coverage (by increasing the number of graphene layers) and the increase in the SERS sensitivity to be achieved as discussed below. The sensitivity is generally decreased with the increase in the number of graphene layers due to the decay of the electromagnetic field through the absorptive graphene thickness with a nonzero imaginary part of the dielectric function,[44] and due to the fact that each graphene layer introduces additional loss resulting from the interband optical absorption of graphene.[45]

A core level shift of +0.6 eV can be observed with respect to the 3d levels of Ag bulk crystals. Positive core level shifts have been observed for metal nanoparticles on substrates, and have been often interpreted in terms of final state effects. For clusters on less conductive substrates (the Ag nanoparticles are on sapphire and the Ag fishnet as Ag intercalated by SiO_2 layers), the positive hole, which is the final state of the photoemission process, can be less efficiently screened, causing a positive core level shift. Electronic structures of very thin metal films are

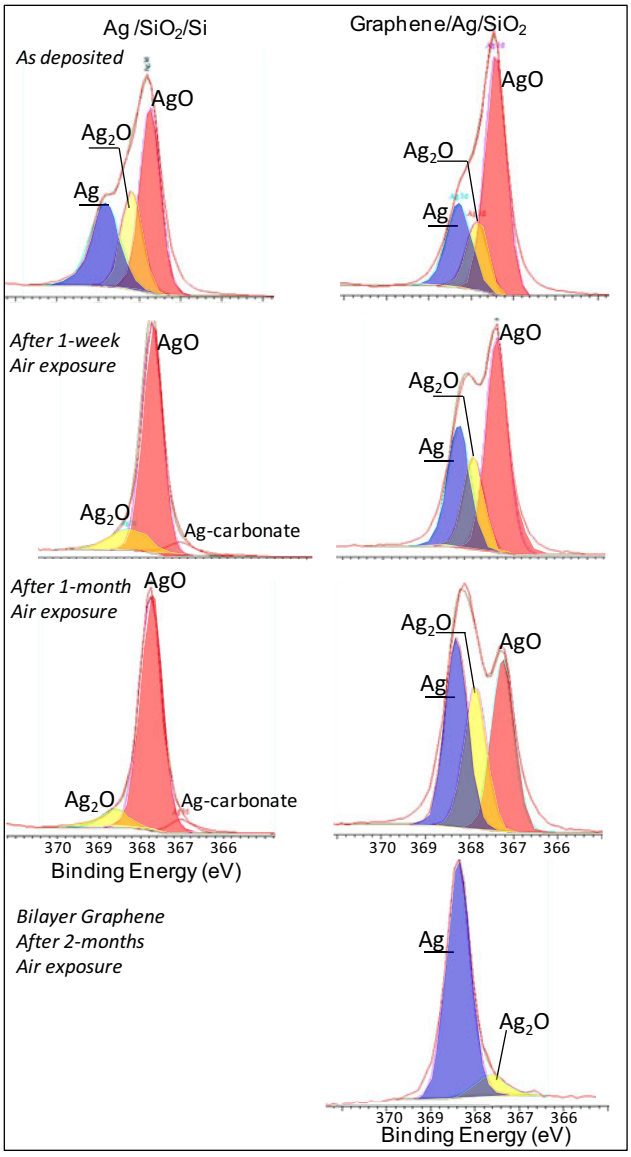

Figure 3. XPS spectra of the Ag3d photoelectron core level for 20 nm Ag deposited on SiO_2/Si and for the graphene/Ag/SiO_2 hybrid acquired soon after sample preparation and after 1-week and 1-month of air exposure; the XPS spectrum for a sample with transferred bilayer graphene and exposed to air for two months is also shown; the Ag-fit components are also indicated.

often modified by substrates, showing core level shifts compared to the respective bulk materials.[46] Another interesting observation is that the metallic Ag^0 component in the Ag 3d5/2 peaks shift to lower binding energies when it is in contact with graphene, from 369.8 eV for Ag deposited on SiO_2 to 369.1 eV, that is, a 0.7 eV shift to lower binding energy results from electron transfer from graphene to Ag. Our results, showing the electron transfer from graphene to Ag, indicate that the doping and charge transfer effect in the graphene/Ag platform can vary (n-type doping of exfoliated graphene on Ag is reported in literature)[23,27] depending on various factors. Naively it is expected that the type and amount of doping depend mainly on the difference between the work functions of free-standing graphene and of the clean metal surface. To explain the observed differences among authors, different values of the Ag work function have been used in computational models describing charge transfer. In addition, while exfoliated graphene is intrinsically undoped, CVD graphene is unintentionally p-type doped shifting the Fermi level down and increasing the work function, which can drive n-type doping by Ag. This is a simplified analysis and first-principles density-functional theory calculations by Khomyakov et al.[47] show that the Fermi level shift in graphene physisorbed on metals like Ag also depends on the graphene–metal surface separation, that is, a separation higher than the equilibrium separation of 3.3 Å, can invert the graphene doping by Ag from n-type to p-type. Small deviations in the graphene–Ag surface distance can occur in real systems due to defects and metal surface topography as can be clearly seen in the tilt SEM images in Figure 1.

Figure 4 displays the C1s and O1s spectra of silver with and without graphene. Before graphene transferring, the C1s spectrum can be fit by a component at 285.0 ± 0.1 eV, due to C-sp3 from adventitious carbon contamination, and a tail peak at 288.3 ± 0.2 eV due to C–O adsorbed on silver from air. When graphene is in contact with silver, new C1s components at 284.3 ± 0.1 eV, due to C-sp2 of graphene, at 286.2 eV due to C–O (epoxy and alkoxy), and at 288.4 eV due to carbonyl

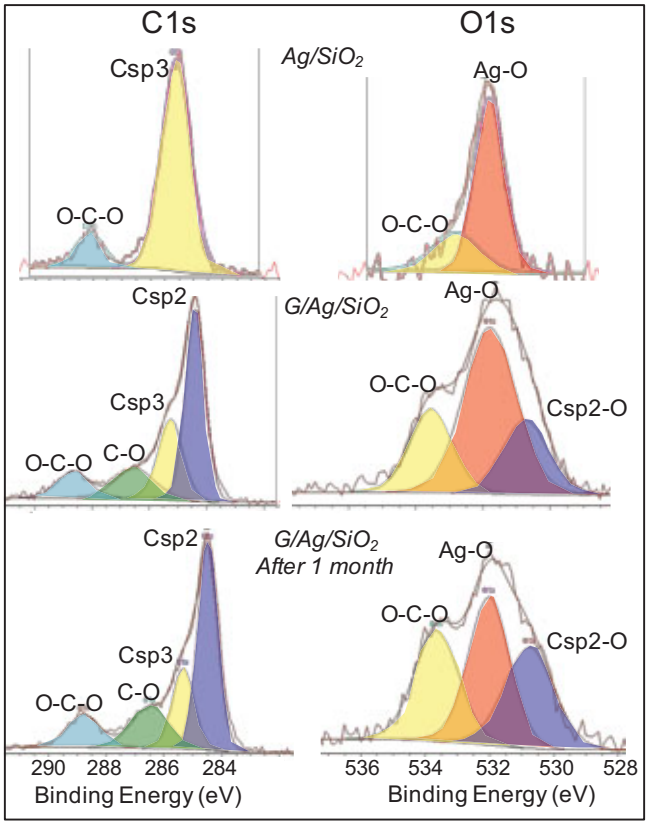

Figure 4. XPS spectra of the C1s and O1s photoelectron core levels for 20 nm Ag deposited on SiO_2/Si without and with graphene ontop (G/Ag/SiO_2), the latter also after one month of air exposure.

C=O, appear.[48] Correspondingly, the O1s photoelectron level of silver without graphene exhibits a dominant component at 531.9 ± 0.1 eV, assigned to metallic oxides, for example, AgO and Ag_2O, and a tail component at 533.1 ± 0.1 eV due to carboxyl groups consistent with the C1s and Ag3d photoelectron core levels. Noteworthy, when silver is coupled to graphene, the O1s component due to metallic silver oxides decreases, while the high energy component at 533.6 eV due to C–O and C=O bonds increases, and an additional component at lower binding energies of 529.9 ± 0.1 eV emerges. The new component in the O1s peak at 529.9 eV has been observed previously in recent work by Vinogradov et al.[49] and by Granas et al.[50] in iridium/graphene intercalated oxygen. Therefore, it can be taken as representative of a small amount of intercalated oxygen patches at the silver-graphene interface or as the formation of an oxygen adatom lattice gas under graphene flakes.[50]

2.2. Rational for the Charge Transfer and Chemical Model

The reduction of the silver oxides enabled by integration with graphene can be understood by considering three factors, that is, the defect sites for oxygen chemisorption, the difference in work function between graphene and silver, and the electrochemical potential of graphene compared to silver. Specifically, graphene defect sites, such as the grain boundaries present in polycrystalline CVD graphene, create catalytic active centers that enhance oxygen chemisorption, thus increasing the reactivity of carbonaceous material in the process of silver deoxidation. Strain enhanced defect reactivity at grain boundaries in graphene is predicted from several simulations.[51,52] Strain at grain boundaries in CVD graphene results from the presence of pentagon, heptagon and octagon rings,[53] which induce inhomogeneous strain, for example, C–C bonds are compressed at the pentagons and are stretched at the heptagons. Additionally, due to van der Waals adhesion to Ag, graphene deforms significantly resulting in local curvature and strain (as shown in Figure 1). The curvature may lead to the rehybridization of sp2 to sp3 bonds (contributing to the D-peak observed in the Raman spectra of Figure 2) and to enhanced reactivity. Computational results demonstrated that a single oxygen atom is inclined to be chemisorbed on the bridge site of a defective graphene surface with exothermic reactions (e.g., binding of oxygen to Stone-Walls defects releases energy of –276 kJ mol^{-1}).[54] In our case, the presence of defects is inferred from the D-peak in the Raman spectra shown in Figure 2.

Additionally, one of the parameters determining the charge transfer is the metal work function, which in the case of the Ag/graphene heterojunction is critical. For Ag, values between 4.2 eV and 4.74 eV have been reported depending on the crystalline orientation but also on the chemical purity. As an example, the work functions of single crystals, determined photoelectrically, were found to be 4.14 ± 0.04 eV, 4.22 ± 0.04 eV and 4.46 ± 0.02 eV for (110), (100), and (111) surfaces of Ag cleaned by Ar sputtering.[55,56] Indeed, contamination and polycrystallinity, relevant to the present case, can increase the work function by several tens of meV, to 4.52 eV, 4,65 eV, and 4.75 eV for the (100), (110), and (111) faces.[56] These are compared with the work function of W_{gr} = 4.55 ± 0.05 eV of single layer graphene and of 4.69 ± 0.05 eV of bilayer graphene,[57] although values as low as 4.42 eV have also been reported.[58] Therefore, considering that evaporated silver thin films are not single crystals, we use the latter set of Ag work function values. Then considering the difference to graphene work function, and the chemical state of silver, electron transfer from the graphene to Ag could occur during the formation of the Ag/graphene composite resulting in a downward shift in the Fermi level in graphene and p-type doping, in agreement with our Raman and XPS observations.

Furthermore, to explain the observed Ag deoxidation, we consider that the reduction potential of AgO ($Ag^{2+} + e \rightarrow Ag^{+} E_0$ = 1.98 V; $Ag^{+} + e \rightarrow Ag$ E_0 = 0.799 V; $Ag_2O + H_2O + 2e \rightarrow 2Ag + 2$ OH- E_0 = 0.342 V) is higher than the reduction potential of graphene (+0.22 V)[59,60] and higher than the reduction potential of molecular oxygen to superoxide involving only a single electron $O_2 + e \rightarrow O_2^{-*}$ (E_0 = –0.16 V)[61] versus SHE (standard hydrogen electrode) as shown by the schematized scale on the right side in **Figure 5**. This allows the injection of electrons from graphene into Ag initiating the following reactions (where graphene is indicated as C∞ and acts as a sort of catalyst for the electron exchange and silver deoxidation and $C\infty_*O_2^-$ indicates the molecular O_2^- anion chemisorbed on a graphene defect site):

$$2\,AgO + e + C\infty \rightarrow 2\,Ag + C\infty_*O_2^- \quad (3)$$

$$AgO + Ag \rightarrow Ag_2O \quad (4)$$

$$C\infty_*O_2^- \leftrightarrow C\infty + O_2 + e \quad (5)$$

The mechanism we describe is based on the concept that graphene functions as an electron transfer catalyst: electron transfer to silver occurs according to the work function difference; in turn, this electron transfer activates, according to electrochemical potentials, the reduction of Ag yielding oxygen chemisorbed at graphene defect sites and grain boundaries, which is further released, as schematized in Figure 5. This proposed mechanism represents a step forward from the simple vision of graphene as solely a passive barrier to oxygen. The model is consistent with the following XPS-based experimental observations: the reduction of AgO and the increase of the Ag metallic component, the presence of Ag_2O as an intermediate product, the decrease of the overall oxygen content, and the additional oxygen component at 529.9 eV. The proposed mechanism is based on the concurrence of all three graphene factors, i.e., the defects acting as sites for chemisorption and transfer of oxygen, the redox potential and the work function of graphene. In light of several studies on GO/Ag and reduced rGO/Ag hybrids (GO = graphene oxide; rGO = reduced graphene oxide),[62] we point out that the same deoxidation of silver oxide cannot apply to GO/Ag for two main reasons: i) the reported work function of 4.9–5.0 eV for graphene oxide (GO) and reduced GO[63–65] is higher than that of graphene and will inhibit charge transfer from graphene to silver for Ag reduction; ii) the presence in GO of hydroxyl and epoxy functional groups on their basal planes in addition to carbonyl and carboxyl groups located at the sheet edges[66] will inhibit the transfer and chemisorption of oxygen at defect sites and, consequently, deactivate the deoxidation of silver. Indeed, better chemical stabilization of silver by CVD graphene has also been recently proposed

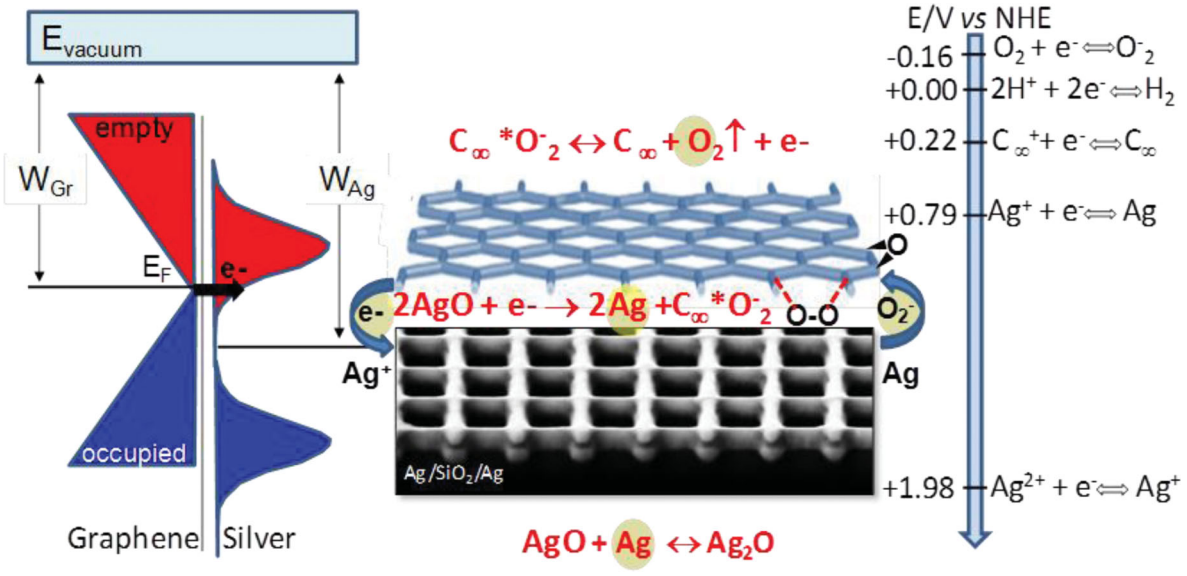

Figure 5. Scheme illustrating the different work function of graphene, W_{Gr}, and polycrystalline silver (also partially oxidized), W_{Ag}, visualizing the electron transfer from graphene to silver, activating the deoxidation of silver using graphene as a catalyst to chemisorb and then remove oxygen. Oxide/epoxyde, C–O bonds formation at graphene (as observed in Figure 4) is also associated with electron injection into silver and reduction of silver oxide; the reduction electrochemical potentials, *E*, are also shown on the right.

by Lee et al.[67] who also investigated the possible passivation of Ag with rGO; they found that the main limitation of r-GO was the insufficient electrical coupling between rGO and nano-size Ag due to the poor conductivity or r-GO (also important for an efficient charge transfer) and non-uniformity.[68]

Additionally, we compare our system with a recent coupling Ag NPs to another metal such as Co, which has created Ag oxidation resistance through a cathodic protection from galvanic coupling to Co used as a sacrificial oxidizing element.[69] While Sachan et al.[69] reported that Ag/Co bimetallic system confers oxidation resistance to Ag for more than seven months, we show below an improvement of Ag NPs plasmonic properties for a period grater than one year of exposure to air.

2.3. Silver/Graphene Hybrids for Plasmonics and Metamaterials

Charge transfer can also be characterized by the variation of the optical properties and the plasma frequency of silver, which are put in evidence through an analysis of the Drude component in the optical spectra.[70] Simultaneously, analysis of the optical spectra allows us to determine the effect of graphene on the functional properties of the graphene/silver composites for plasmonic applications. To this aim, we have recorded, in the 0.75–6.5 eV photon energy range, spectra of the complex pseudodielectric function, $\langle\varepsilon\rangle = \langle\varepsilon_1\rangle + i\langle\varepsilon_2\rangle$, of a thin Ag film,[71] of the Ag nanoparticles ensemble, and of the Ag fishnet structure with and without integrated graphene. **Figure 6** shows the spectra of the real, $\langle\varepsilon_1\rangle$, and imaginary, $\langle\varepsilon_2\rangle$, parts of the pseudodielectric function of a 50 nm evaporated film with and without graphene, the latter also after air oxidation. The Ag films exhibited dielectric functions with a larger negative real component $\langle\varepsilon_1\rangle$. Conversely, the lower $\langle\varepsilon_2\rangle$ indicates lower energy loss, which is important to enhance the propagation length of surface plasmons. The dielectric function of silver is approximated by a Drude-Lorentz model[70]

$$\varepsilon(\omega) = 1 - \frac{\omega_p^2}{\omega^2 - i\gamma\omega} + \frac{f\omega_L^2}{\omega_L^2 - \omega^2 + iT_L\omega}$$

with

$$\omega_p = 9.17\,\text{eV},\ \gamma = 0.021\,\text{eV},\ f = 2.2,\ \omega_L = 5.27\,\text{eV},\ \Gamma_L = 1.14\,\text{eV}$$

where, ω_p and γ (ω_L and Γ_L) are the plasma frequency and collision frequency in the Drude (Lorentz) term. The Lorentz term accounts for the interband transitions of silver above 3.8 eV. Focusing on the Drude part, data in Figure 6 show that the decrease of the plasma frequency and the increase of the Drude damping factor, γ, can originate from the chemical interface effect due to oxidation of silver.[70] Conversely, the effect of graphene on Ag should be to increase the plasma frequency through electron transfer to Ag (consistent with XPS and Raman data) and/or a decrease in the scattering and hence of the damping factor due to inhibited oxidation.

Of most importance is the observation that graphene shifts Ag towards a "perfect metal", which is defined as having an infinitesimally small damping ($\gamma -> 0$). The vanishing absorption $\gamma -> 0$ yields a δ-function like $\varepsilon_2(\omega)$, such that at low, but nonzero frequencies the absorption is reduced. As can be clearly seen in Figure 6, the pseudodielectric function, $\langle\varepsilon\rangle = \langle\varepsilon_1\rangle + i\langle\varepsilon_2\rangle$, of silver covered by graphene has the smallest $\langle\varepsilon_2\rangle$, and is thereby the least lossy material combination, which shows up also in the fitting of γ for all three samples, specifically $\gamma_{Ag} = 0.05$, $\gamma_{AgO} = 0.20$, and $\gamma_{Ag} = 0.03$. The same effect can be observed in Figure 6 over the energy range of 3.4 to 4.2 eV:

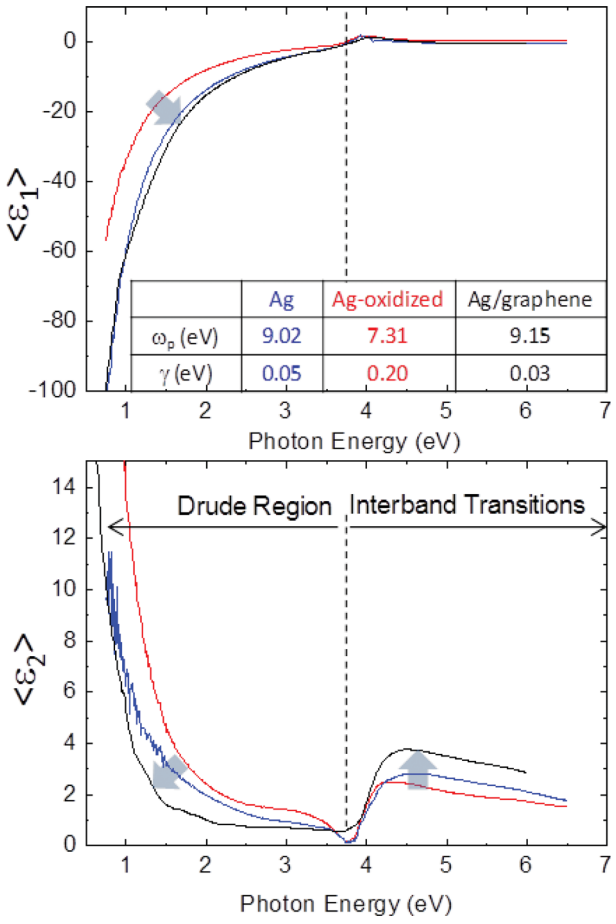

Figure 6. Spectra of the real, ε_1, and imaginary, ε_2, parts of the pseudodielectric function of a 50 nm evaporated Ag film with and without graphene, the latter also after air oxidation. The values of the plasma frequency, ω_p, and collision frequency (damping factor) of the Drude term are also shown for freshly evaporated silver, oxidized silver and silver with graphene transferred ontop.

for the Ag intraband transition, graphene enhances the oscillator strength, (grey line) by enhancing the f parameter from 2.2. to 2.6. and slightly reducing the Γ_L parameter from 1.14 to 0.86.

The optical analysis has been extended to graphene integrated self assembled Ag nanoparticles (NPs) on Al_2O_3. **Figure 7** shows the extinction coefficient spectra of Ag NPs with and without graphene. The optical spectra of the nanoparticle arrays were measured over a period of one year of air exposure to study the effectiveness of the graphene passivation. The extinction coefficient, <*k*>, and refractive index, <*n*>, spectra of our transferred CVD graphene are also shown. The graphene extinction coefficient spectrum is characterized by the Van Hove peak[45] at 4.8 eV, which is a combination of the collective oscillation of the π-electron system due to the $\pi \rightarrow \pi^*$ transition of the aromatic C–C bond along the M-direction of the Brillouin zone of graphene and of the so-called π-plasmon. Figure 7 shows that the as-deposited Ag NPs supported on an Al_2O_3 substrate have a localized plasmon resonance (LSPR) peak at approximately 3 eV. Over a four-months period, the resonant peak damped dramatically for unpassivated Ag NPs. In contrast, the Ag NPs that were covered by the graphene showed a much more intense and robust preservation of the initial plasmonic properties. The variation of the amplitude and red-shift in λ_{max} of approximately 0.15 eV was due to the higher refractive index of the graphene layer,[72] since integration with high index materials increases the extinction cross-section. No significant damping was observed after one year of air exposure for the graphene/Ag NPs sample, indicating that graphene was effective in inhibiting Ag NPs oxidation and preserving stable plasmonic properties. Noteworthy, our shift and damping is negligible after almost a year of air exposure, whereas in the literature,[30] only a month of air exposure was used to for testing the stability.

Graphene has also been transferred on an Ag fishnet structure fabricated to create main resonances and a metamaterial in the visible.[31] The optical properties have been measured by transmission and ellipsometry before and after the graphene passivation. **Figure 8** shows the transmittance spectra of the Ag fishnet as fabricated, with graphene and for the latter also after one year of air exposure. The graphene results in a blue-shift of the main resonance (this blue-shift has also been observed in the ellipsometric spectra of the ellipsometric variables Ψ and Δ and is therefore a characteristic of the hybrid Ag/graphene). Figure 8b also compares transmission experimental and simulated data, which have been obtained by using an exact Maxwell solver (rigorous coupled wave analysis, RCWA).[73] The agreement between the measured red curve and the simulated blue curve (converged) is remarkable.

2.4. SERS Functionality

The stability of the plasmon resonance of the Ag NPs and fishnet structure is relevant to the realization of more stable and robust SERS sensors. Silver is often selected to fabricate SERS substrates for the detection of biomolecules because of its high SERS activity.[14] Commonly, the encapsulation of silver in SiO_2 and polymer is used to improve the stability and biocompatibility of the SERS substrates, which however, reduces the sensitivity. Recently self-assembled graphene oxide/Ag NPs hybrids have been demonstrate as SERS substrates.[74] Therefore, we have tested the functional SERS activity of the CVD graphene coupled to the Ag fishnet and to Ag NPs by measuring SERS spectra using benzyl thiol, also known as benzyl mercaptan (BZM), as the probe molecule, where the graphene can adsorb the target molecules and Ag NPs and Ag fishnet supply strong SERS activity. A comparison between the fishnet and NPs is made also to understand the effects related to an ordered periodic structure versus a random ensemble of nanoparticles. Here, the choice of BZM is because it is a simple molecule that can adsorbe on graphene either through π–π^* interaction of aromatic rings in a planar geometry or thiol groups via unsaturated bonds at grain boundaries. We are also investigating and detecting SERS effect of graphene/metal NPs using other molecules without thiol group, such as hemin (a porphyrin) and Crystal Violet (CV), extending the applicability of graphene/metal NPs hybrids to other molecules, and will report on these findings in another publication.

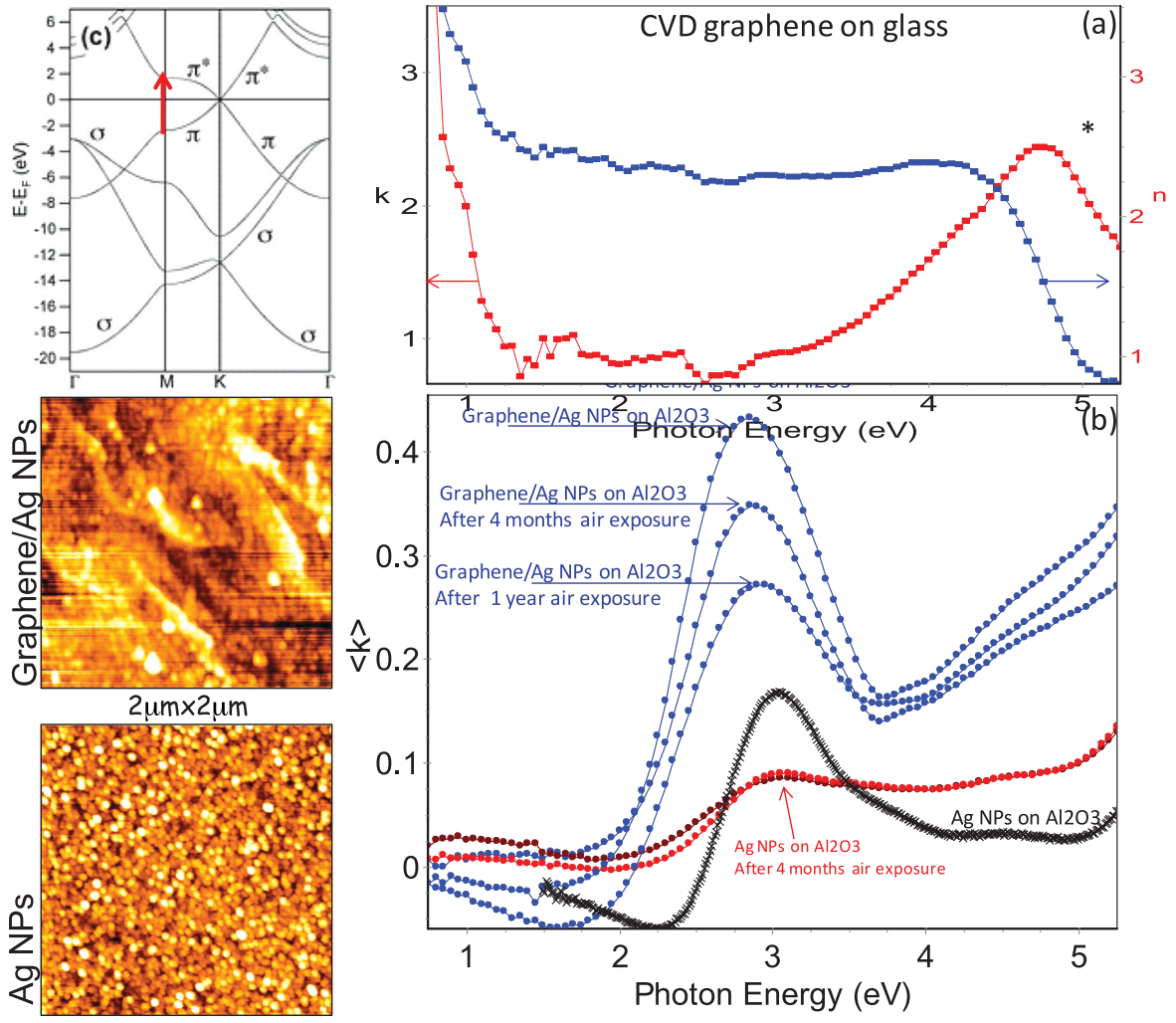

Figure 7. Pseudoextinction coefficient, <*k*>, and pseudorefractive index, <*n*>, spectra of the CVD graphene (up panel) with the corresponding sketch of the graphene band diagram, and extinction coefficient spectra of the Ag NPs (bottom panel) on Al2O3 substrate with and without graphene also as a function of exposure to air over 1 year. The 2 μm × 2 μm AFM images of Ag NPs with and without graphene are also shown.

Figure 9 shows the SERS spectra of BZM adsorbed on graphene on glass, on the graphene/Ag-NPs and on the graphene/Ag-fishnet taken using a He/Ne laser at 632.8 nm as the excitation source. It has to be mentioned that no BZM Raman peak is observed when BZM is dropped onto graphene or the naked Ag nanostructures without graphene, in the latter case presumably because of the silver oxidation as discussed previously. While full assignment of peaks can be found in ref. [75], **Table 1** summarizes the main mode we observed for both BZM and graphene. The peaks at 1601 and 1001 cm^{-1} are due to the ring CC stretching (ν8a), and the ring CCC in-plane bending (ν12) modes of BZM, respectively.[76]

For the SERS spectra on graphene/Ag hybrids, the absence of the *ν*(SH) stretching band at 2569 cm^{-1} appeared in the ordinary Raman (OR) spectrum indicates that BZM is chemisorbed on the surfaces by rupture of the S–H bond. Simultaneously, the C–S band at 678 cm^{-1} may indicate that the BZM chemisorbes at point defects of graphene whose presence is inferred by the D-band at 1312 cm^{-1}, and possibly the same C–O centers (epoxy of carbohydroxyl centers formed on graphene by the silver deoxidation (see scheme in Figure 5). The position of the *ν*8a band of BZM on silver appeared at 1589 cm^{-1}, while it appeared at 1601 cm^{-1} in the liquid state. The decrease in frequency also of the ring breathing *ν*12 mode from ≈1001 cm^{-1} to 988 cm^{-1}, as well as of the other BZM ring modes, when on graphene/Ag hybrids implied a direct ring *π* orbital interaction with graphene. These results suggest a flat orientation of the phenyl ring in BZM on graphene induced by the electron interaction between graphene and the BZM *π** antibonding orbitals affecting the C–C stretching (*π*-stacking). Noteworthy, a difference in SERS spectra is seen for coupling to Ag fishnet and to Ag NPs, that is, in the case of BZM/Graphene/Ag NPs all in-plane modes of BZM are seen in the SERS spectrum, whereas only the C–C ν12 in-plane mode is seen for BZM/Graphene/Ag fishnet.

Assuming graphene as an electron shuttle, the deposition of graphene on partially oxidized Ag NPs as well as on Ag fishnet structures has drastic effects. A strong field enhancement can

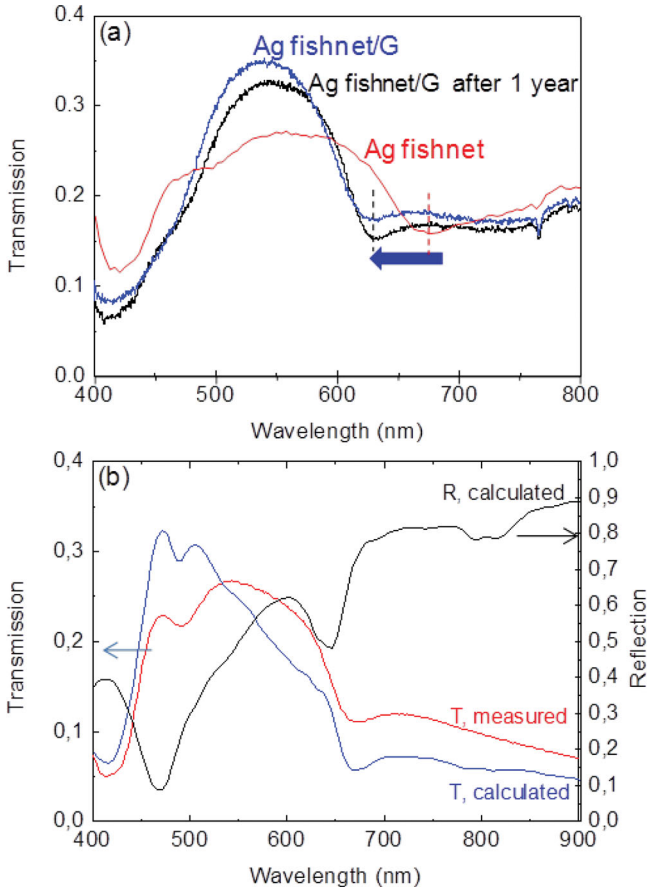

Figure 8. a) Transmission spectra of the Ag fishnet without (red curve) and with (blue curve) graphene and the latter after one year of air exposure (black curve). b) Comparison between measured and RCWA calculated transmission and refection curves for the as-deposited fishnet.

take place only on a metallic surface since all of the field lines have to be perpendicular to the surface, and if the radius of curvature (RoC) is small (for convex surfaces), the field will be enhanced drastically and even diverge for $r->0$. On a dielectric sphere the field will increase, too, but just given by the polarization of the dielectric sphere and will remain finite. We checked this prediction using the probe molecule BZM. The increase in intensity of the Raman signal for adsorbates on particular surfaces is either assigned in the literature to electromagnetic (EM) field enhancements or chemical shifts, caused by a partial charge transfer. For our structures we assume that the major role is due to EM field enhancement. It is clear that on the Ag fishnet localized surface plasmons are excited. The rigorous coupled wave analysis (RCWA) yields enhancement factor of up to 50 on the sharp convex (outer) edges of the fishnet structure, in the inner metallic edges the field is reduced,[77] as shown in **Figure 10**. The field enhancement depends quadratically on the inverse RoC of the fishnet structure, so at very sharp outer edges or tips, with a radius of curvature of less than 1 nm it could even be 2–3 orders of magnitude enhanced. Our fishnets are probably as not as sharp and we estimated the RoC from SEM measurements to be ≈3–5 nm.

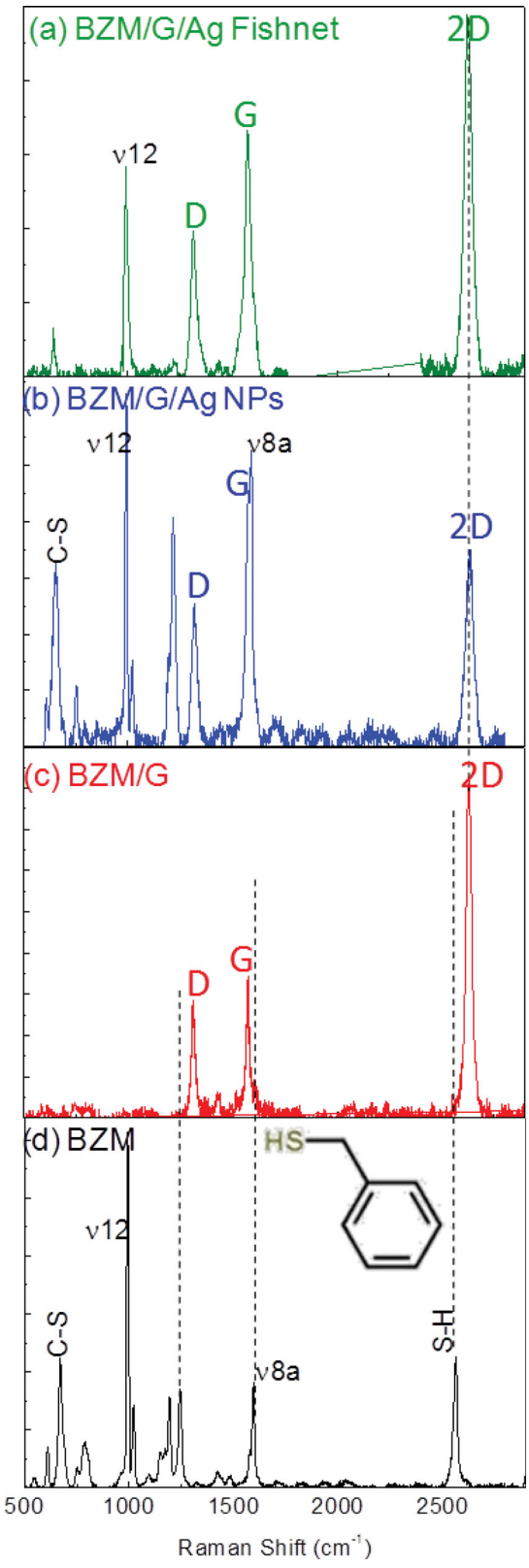

Figure 9. Raman spectra obtained using 633 nm radiation as an excitation soure: a) SERS spectrum of BZM on graphene/Ag fishnet; b) SERS spectrum of BZM on graphene/Ag NPs; c) BZM on graphene on glass; and d) ordinary spectrum of liquid BZM.

Table 1. Vibrational assignment of BZM and graphene for data in Figure 9.

OR [cm^{-1}]	Ag SERS [cm^{-1}]	Assignment
In-plane BZM		
1601	1589	8a(A_1)
1201	1191	13(A_1)
1029	1013	18a(A_1)
1001	988	12(A_1)
795	777	1(A_1)
618		6b(B_2)
Side-chain BZM		
2569	-	ν(SH)
1252	1222	γ(CH_2) (wagging or twist)
678	652	ν(CS)
Graphene		
2632	2639	2D-band
1577	1581	G-band
1312	1318	D-band

The stimulated Raman signal (a third order nonlinear process), however, is influenced by the field enhancement twice: first, the field enhancement magnifies the field a factor of F, the intensity a factor of F^2. As it is a nonlinear process, the intensity acts back on the excitation of the Raman modes of the molecule, therefore the total SERS signal is also increased by a factor F^2, and the total enhancement is of order of F^4. For a thorough theoretical description of SERS as a nonlinear optical process the reader is referred to elsewhere.[78]

The geometrical complicated structure of the fishnet not only provides resonances (or in other words an increased photonic density of states) for the incident laser field with frequency ω_i, but also, due to its geometry, for $\omega_i \pm \omega_v$ where ω_v stands for the different vibrational bands of the BZM. Because the measured Raman shifts are of the order of 1000 cm^{-1}, and thereby rather small (υ_{12} $\omega_i \pm \omega_v \approx 0.12$ eV) against the incident photon energy, we can assume that in the fishnet structure the low wavenumber Raman active modes are enhanced the same factor. This is true for the C–S and mode, but the 1250 cm^{-1} mode is not enhanced the same amount, probably because other resonance conditions apply. Finally we assume that the Ag NPs display even more BZM modes as a result of the statistical distribution of the NP sizes. Different Ag NPs have different RoCs, but of even greater importance is the effect of the different sizes of NPs which are resonant with different frequency shifts, thereby delivering a multitude on signals. On a flat graphene layer, however, all these Stokes lines are undetectable.

Finally, to determine the SERS enhancement, EF, we considered the ν12 mode appearing in both the G/Ag NPs and G/Ag fishnet and found EF values of 210 for the graphene/Ag fishnet and of 290 for the graphene/Ag NPs. These EF values are the average values reproducibly measured in various points across the sample, and are not the highest values that can be achieved at hot spots. Noteworthy, for comparison a CVD graphene transferred on a similar Au fishnet has demonstrated an enhancement factor of ≈40 for the methylene blue.[79]

Some considerations about the origin of this enhancement could be inferred in light of previous works on graphene as a platform for SERS. Dresselhaus' group has demonstrated, using various molecules on graphene Raman probed with various laser sources, that graphene Raman enhancement factors in a range 2–17 can be obtained by the chemical mechanism (CM) that is based on charge transfer.[80] In our case, the reason why we do not observe BZM Raman signals when adsorbed on graphene (without Ag) could be because the CM is not active since electrons are transferred to Ag underneath for the deoxidation. Therefore, the observed SERS for the BZM/graphene/Ag may be ascribed to the electromagnetic mechanism (EM). However, the EF values are not as high as those typically expected (>10^4) for the EM. This could be due to the reduction of the electromagnetic field by the graphene thickness/absorption, to averaging observed across the surface, and also to the imperfect graphene-veiling of Ag NPs and fishnet (as shown in tilt SEM in Figure 1), the latter factor being important as recently demonstrated by Xu et al.[81]

3. Conclusion

In summary, we have demonstrated that coupling graphene with partially oxidized silver is effective in silver deoxidation. Graphene was grown by CVD and transferred onto silver nanoparticles and periodic fishnet nanostructures. Defects created by the processing act as sites for the detachment of oxygen and silver oxidation. According to XPS and Raman experimental observations and in agreement with data of electrochemical potentials for graphene, silver and oxygen and of their work functions, we formulate a silver deoxidation mechanism based on the electron transfer to silver catalyzed by graphene and on the cathodic silver protection arising from galvanic coupling to graphene. It has also been demonstrated that graphene is effective in improving the stability of the localized plasmon resonance in the visible range of silver nanoparticles and fishnets for longer than one year. Furthermore, considering that graphene is known to be strongly sensitive to contamination, for example, is p-doped by water vapor in the air, and that humidity could produce changes of graphene that may affect the stability of silver, it is pointed out that data shown in Figures 7,8 have been measured after exposing the samples over time to different humidity levels in different ambients associated with the various laboratories of co-authors, achieving reproducible measurements of the optical characteristics and only a 10% change in the sheet resistance was measured on graphene after humidity exposures.

Thus, graphene/silver hybrids based LSPR applications and SERS sensors can be significantly more stable and useful, especially over a long time period, enabling the technological development of stable plasmonic and metamaterials toward lower wavelengths.

Finally, the SERS functionality as SERS sensors of graphene/Ag-nanoparticles and graphene/Ag-fishnet has been evaluated and compared using the BZM thiol as probing molecule, whose

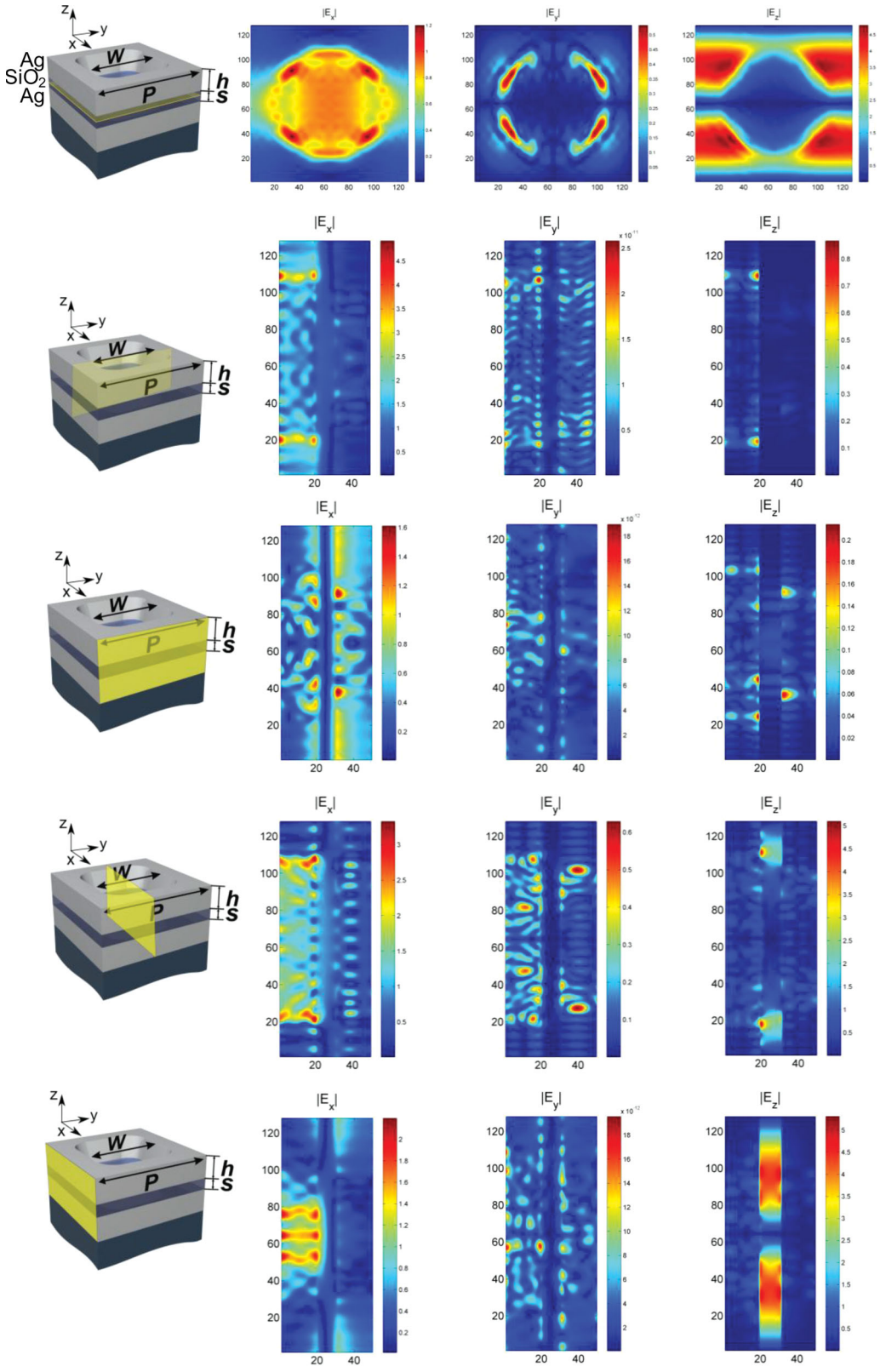

Figure 10. Electromagnetic field enhancement calculated along the three directions, *Ex*, *Ey*, and *Ez*, at various points indicated by the yellow shadowed area for the Ag fishnet with period 200 nm. Layer stack is 30 nm Ag (*h*)/15 nm SiO_2 (*s*)/30 nm Ag. *E* is polarized in *x* direction. Fields are calculated at the $\lambda = 670$ nm resonance dip.

π-system can electronically interact with that of graphene. Because of this interaction, only the in-plane mode of BZM is SERS active for graphene/Ag-fishnet; conversely, more BZM Raman modes are SERS active using graphene/Ag-nanoparticles hybrids. A rational for the different SERS response of the two hybrid systems is also provided by electromagnetic field calculations by RWCA. Interestingly, the same SERS spectra have been recorded after 4 months of air exposure of the graphene/Ag-fishnet and graphene/Ag-nanoparticles samples, indicating the stability of the graphene hybrids in providing stable and reusable SERS sensors.

4. Experimental Section

Graphene Growth: Graphene was grown by chemical vapor deposition (CVD) from mixtures of CH_4:H_2 on copper[71] and then transferred onto silver films and fishnet structures using the thermal tape method.[21] Specifically, the thermal tape was bound to graphene, and the copper was etched in a solution (0.1 M in distilled water) of ammonium persulfate (APS); the graphene/tape carrier was rinsed in isopropanol and dried first in N_2 atmosphere and subsequently kept in ultra high vaccum pumping (UHV) to eliminate traces of humidity and transferred on silver structures and films and the tape released by heating to 90 °C in N_2 atmosphere. This temperature is low enough to prevent any re-aggregation and change of morphology of the Ag NPs as well as of the Ag fishnet.[31] Finally, to remove any possible tape residue/contamination the hybrid graphene/Ag samples were dipped in an optimized mixture of solvents for 20 min and then dried again by a UHV pumping with the sample at 90 °C to further remove any solvent residual. XPS chemical analysis on a control graphene sample demonstrated that this procedure does not give any residual copper and tape or solvent contamination. The absence of contaminations was also checked optically by spectroscopic ellipsometry, since recently we have demonstrated[82] that this technique could reveal unexpected absorption by contamination/impurities. Thus, an impurity/contamination-free graphene/silver interface is formed.

Silver Nanostructures Fabrication: Ag ultrathin films and Ag nanoparticles were evaporated on Si/SiO_2 wafer and on Al_2O_3 substrates.

For fabrication of the Ag fishnet herein discussed, nanoimprint lithography (NIL) masters were fabricated on a 4" silicon wafer by e-beam lithography. A diluted Ormocere layer is spin coated on top of a lift-off resist (LOR) and structured using NIL. The Ormocere contains not only organic but also inorganic materials resulting in a much lower etching rate than the used LOR layer underneath. Therefore, when using this material combination recessed sidewalls are achieved in a simple RIE etching step without the need of a wet chemical development step of the LOR layer. The different layers of Ag (by evaporation) and of SiO_2 (by sputtering) were deposited to fabricate the structure used here, which consisted of a layer stack of 30 nm Ag / 15 nm SiO_2 / 30 nm with an Ag lines period of 200 nm.

SERS Experiment: BZM was purchased from Sigma–Aldrich and was used without further purification forming a solution in CH_2Cl_2. The concentration of BZM in the colloidal solution was $\approx 5 \times 10^{-4}$ M. The solution was dropcasted on the Ag NPs and fishnet with and without graphene; the samples after 6 h were rinsed in CH_2Cl_2 and dried in N_2.

Characterization. The effects of the topographical characteristics of the silver nanostructures were investigated by field-emission scanning electron microscope (FE-SEM). Morphology analysis was carried out with an atomic force microscope (AutoProbe-CP ThermoMicroscope) using a gold coated Si tip with a resonant frequency of 80 kHz.

Chemical analysis was carried out by X-ray photoelectron spectroscopy (XPS). A high resolution X-ray photoelectron spectrometer (Kratos) was used to investigate the chemical state, the silver–oxygen chemical states and the effect of graphene on oxidation of silver in time. All XPS measurements were made at room temperature using crystal-monochromatised AI Ka radiation. Samples after preparation were transferred immediately to the XPS to minimize air exposure. The analysis of the main photoelectron peaks of Ag3d, O1s, C1s in addition to the valence band is used to track chemical and electronic changes in silver and graphene layers. Specifically, the Ag3d and O1s give information on the chemical states of Ag, Ag_2O and AgO, while the C1s photoelectron peak is used to analyze graphene modifications. The valence band analysis was useful to investigate Fermi level shifts and, hence, charge transfer between graphene and silver. The XPS system has a video camera and grid system and a spot on the sample of 500 μm × 600 μm, which is of comparable size to the 700 μm × 700 μm sampling are of Raman with a 10× objective which helped us in identifying region of the samples without holes or cracks of the order of tens of micron or higher; the same regions were then samples by XPS.

Microstructural analysis was performed by Raman spectroscopy. Raman spectroscopy has shown to be a powerful tool to assess thickness and quality of graphene layers.[83] Raman spectra were then collected using a LabRAM HR Horiba-Jobin Yvon spectrometer equipped with the 632.8 nm, 532 and 473 nm excitation lasers. Graphene Raman and SERS measurements were run under ambient conditions at low laser power (0.5 mW for 632.8 nm and 0.2 mW for 532 nm) to avoid laser-induced heating and damage. A 50× objective (numerical aperture (NA) = 0.75) was used for all of the measurements. The Raman band of a silicon wafer at 520 cm^{-1} was used to calibrate the spectrometer, and the accuracy of the spectral measurement was estimated to be better than 1 cm^{-1}.

The SERS enhancement factor, EF, was calculated according to $EF = (I_{SERS}/N_{SERS})/(I_{Raman}/N_{Raman})$, which represents the ratio between the SERS and Raman BZT signal intensities, I_{SERS} and I_{Raman}, both normalized for the number of probed molecules, N_{SERS} and N_{Raman}. The number of molecules, N_{SERS}, probed in graphene/Ag samples was estimated under the approximations that the graphene surface is fully covered by a monolayer of BZM molecules lying flat on the surface by π–π stacking and that the surface covered by a BZM molecules is a circular area with diameter equal to the expected BZM length (0.55 nm).[84] Thus, N_{SERS} was calculated by dividing the laser irradiated graphene area (πr_{laser}^2,with r laser = $0.61\lambda_{laser}$/NA) by the area occupied by a single BZM molecules, and N_{Raman} was calculated by considering the irradiated BZM solution volume (estimated as the product of laser spot area and the laser spot depth of focus,$\approx 2\lambda/NA^2$) and its concentration (4.0 M).

Optical analysis was carried out by reflection and transmission measurements and also by spectroscopic ellipsometry.[71] Spectroscopic ellipsometry recorded the corresponding plasmonic response of the fishnet structures by directly recording the pseudodielectric function $\langle\varepsilon\rangle = \langle\varepsilon_1\rangle + i\langle\varepsilon_2\rangle$, which is related to the extinction coefficient k and refractive index n of structure by the following equation

$$\langle\varepsilon\rangle = \langle\varepsilon_1\rangle + i\langle\varepsilon_2\rangle = \sin^2\theta\left[1 + \tan^2\theta\frac{(1-\rho)^2}{(1-\rho)^2}\right] = \langle(n + ik)^2\rangle$$

where θ is the angle of incidence fixed at 70° and ρ is the complex reflection coefficient for the parallel, r_p, and perpendicular, r_s, polarizations, defined as

$$\rho = \frac{r_p}{r_s} = \tan\Psi * e^{i\Delta}$$

where $\tan\Psi$ represents the change of amplitude of the reflected polarized light beam with respect to the linearly polarized incident beam, while the phase change between the two polarizations is related to cos Δ. Ellipsometric spectra were acquired using a phase-modulated spectroscopic ellipsometer (UVISEL, Horiba Jobin Yvon) in the 180–1700 nm spectral range with 1 nm resolution.

Acknowledgements

The authors acknowledge funding by the European Community's 7th Framework Programme under grant agreements no 228637 NIM_NIL (www.nimnil.org) and no. 314578 MEM4WIN.

Received: September 9, 2013
Published online: November 19, 2013

[1] S. A. Maier, M. L. Brongersma, P. G. Kik, S. Meltzer, A. A. G. Requicha, H. A. Atwater, *Adv. Mater.* **2001**, *13*, 1501–1505.
[2] A. J. Haes, R. P. Van Duyne, *J. Am. Chem. Soc.* **2002**, *124*, 10596–106043.
[3] K. S. Novoselov, A. K. Geim, S. V. Morozov, D. Jiang, M. I. Katsnelson, I. V. Grigorieva, S. V. Dubonos, A. A. Firsov, *Nature* **2005**, *438*, 197–200.
[4] H. Chan, H. Wu, *Adv. Funct. Mater.* **2013**, *23*, 1984–1997.
[5] W. Tu, Y. Zhou, Z. Zou, *Adv. Funct. Mater.* **2013**, 23, 4996–5008
[6] M. H. Liang, L. J. Zhi, *J. Mater. Chem.* **2009**, *19*, 5871–5878.
[7] I. P. Murray, S. J. Lou, L. J. Cote, S. Loser, C. J. Kadleck, T. Xu, J. M. Szarko, B. S. Rolczynski, J. E. Johns, J. Huang, *J. Phys. Chem. Lett.* **2011**, *2*, 3006–3012.
[8] G. V. Naik, V. M. Shalaev, A. Boltasseva, *Adv. Mater.* **2013**, *25*, 3264–3294.
[9] A. Vakil, N. Engheta, *Science* **2011**, *332*, 1291–1294.
[10] W. Zhou, J. Lee, J. Nanda, S. T. Pantelides, S. J. Pennycook, J. C. Idrobo, *Nat. Nanotechnol.* **2012**, *7*, 161–165.
[11] F. H. L. Koppens, D. E. Chang, F. J. García de Abajo, *Nano Lett.* **2011**, *11*, 3370–3377.
[12] J. H. Park, P. Ambwani, M. Manno, N. C. Lindquist, P. Nagpal, S.H. Oh, C. Leighton, D. J. Norris, *Adv. Mater.* **2012**, *24*, 3988–3992.
[13] W. Wei, K. Chen, G. Ge, *Adv. Mater.* **2013**, 25, 3863-3868.
[14] N. L. Dmitruk, S. Z. Malynych, I. E. Moroz, V. Yu. *Quantum Electron. Optoelectron.* **2010**, *13*, 369–373.
[15] G. Dolling, M. Wegener, C. M. Soukoulis, S. Linden, *Opt. Lett.* **2007**, *32*, 53–55.
[16] O. S. Ivanova, F. P. Zamborini, *J. Am. Chem. Soc.* **2009**, *132*, 70–72.
[17] Standard Thermodynamic Properties of Chemical Substances, http://www.update.uu.se/~jolkkonen/pdf/CRC_TD.pdf (accessed: November, **2013**).
[18] J. Schmitt, P. Machtle, D. Eck, H. Mohwald, C. A. Helm, *Langmuir* **1998**, *15*, 3256–3266.
[19] Y. Han, R. Lupitskyy, T. M. Chou, C.M. Stafford, H. Du, S. Sukhishvili, *Anal. Chem.* **2011**, *83*, 5873–5880.
[20] T. Gokus, R. R. Nair, A. Bonetti, M. Bohmler, A. Lombardo, K. S. Novoselov, A. K. Geim, A. C. Ferrari, A. Hartschuh, *ACS Nano* **2009**, *3*, 3963–3968.
[21] S. Chen, L. Brown, M. Levendorf, W. Cai, S. Y. Ju, J. Edgeworth, X. Li, C. W. Magnuson, A. Velamakanni, R. D. Piner, J. Kang, J. Park, R. S. Ruoff, *ACS Nano* **2011**, *5*, 1321–1327.
[22] Q. Yu, L. A. Jauregui, W. Wu, R. Colby, J. Tian, Z. Su, H. Cao, Z. Liu, D. Pandey, D. Wei, T. F. Chung, P. Peng, N. P. Guisinger, E. A. Stach, J. Bao, S. S. Pei, Y. P. Chen, *Nat. Mater.* **2011**, *10*, 443–449.
[23] G. Giovannetti, P. A. Khomyakov, G. Brocks, V. M. Karpan, J. Brink, P. J. Kelly, *Phys. Rev. Lett.* **2008**, *101*, 026803.
[24] X. Zhou, X. Huang, X. Qi, S. Wu, C. Xue, F. Y. C. Boey, Q. Yan, P. Chen, H. Zhang, *J. Phys. Chem. C* **2009**, *113*, 10842–10846.
[25] L. Zhang, C. Jiang, Z. Zhang, *Nanoscale* **2013**, *5*, 3773–3779.
[26] W. Yuan, Y. Gu, L. Li, *Appl. Surf. Sci.* **2012**, *261*, 753–757.
[27] J. Lee, K. S. Novoselov, H. S. Shin, *ACS Nano* **2011**, *5*, 608–612.
[28] T. Wu, H. Shen, L. Sun, B. Cheng, B. Liu, J. Shen, *ACS Appl. Mater. Interfaces* **2012**, *4*, 2041–2047.
[29] Y. Ren, S. Chen, W. Cai, Y. Zhu, C. Zhu, R. S. Ruoff, *Appl. Phys. Lett.* **2010**, *97*, 053107.
[30] J. C. Reed, H. Zhu, A. Y. Zhu, C. Li, E. Cubukcu, *Nano Lett.* **2012**, *12*, 4090–4094.
[31] M. Losurdo, I. Bergmair, M. M. Giangregorio, B. Dastmalchi, G. V. Bianco, C. Helgert, E. Pshenay-Severin, M. Falkner, T. Pertsch, E. Bernhard Kley, U. Huebner, M. A. Verschuuren, M. Muehlberger, K. Hingerl, G. Bruno, *J. Phys. Chem. C* **2012**, *116*, 23004–23012.
[32] J. Tian, H. Cao, W. Wu, Q. Yu, N. P. Guisinger, Y. P. Chen, *Nano Lett.* **2012**, *12*, 3893–3899.
[33] A. Reina, X. Jia, J. Ho, D. Nezich, H. Son, V. Bulovic, M. S. Dresselhaus, J. Kong, *Nano Lett.* **2009**, *9*, 30–35.
[34] A. Das, S. Pisana, B. Chakraborty, S. Pisacane, S. K. Saha, U. V. Waghmare, K. S. Novoselov, H. R. Krishnamurthy, A. K. Geim, A. C. Ferrari, A. K. Sood, *Nat. Nanotechnol.* **2008**, *3*, 210–215.
[35] D. L. Duong, G. H. Han, S. M. Lee, F. Gunes, E. S. Kim, S. T. Kim, H. Kim, Q. H. Ta, K. P. So, S. J. Yoon, S. J. Chae, Y. W. Jo, M. H. Park, S. H. Chae, S. C. Lim, J. Y. Choi, Y. H. Lee, *Nature* **2012**, *490*, 235–239.
[36] T. M. G. Mohiuddin, A. Lombardo, R. R. Nair, A. Bonetti, G. Savini, R. Jalil, N. Bonini, D. M. Basko, C. Galiotis, N. Marzari, K. S. Novoselov, A. K. Geim, A. C. Ferrari, *Phys. Rev. B* **2009**, *79*, 205433.
[37] Z. H. Ni, T. Yu, Y. H. Lu, Y. Y. Wang, Y. P. Feng, Z. X. Shen, *ACS Nano* **2008**, *2*, 2301–2305.
[38] T. Yu, Z. Ni, C. Du, Y. You, Y. Wang, Z. Shen, *J. Phys. Chem. C*, **2008**, *112*, 12602–12605.
[39] M. Huang, H. Yan, C. Chen, D. Song, T. F. Heinz, J. Hone, *Proc. Natl. Acad. Sci. U. S. A.* **2009**, *106*, 7304–7308.
[40] W. X. Wang, S. H. Liang, T. Yu, D. H. Li, Y. B. Li, X. F. Han, *J. Appl. Phys.* **2011**, *109*, 07C501.
[41] K. S. Subrahmanyam, A. K. Manna, S. K. Pati, C.N.R. Rao, *Chem. Phys. Lett.* **2010**, *497*, 70–75.
[42] T. W. H. Oates, M. Losurdo, S. Noda, K. Hinrichs, *J. Phys. D: Appl. Phys.* **2013**, *46*, 145308.
[43] J. F. Weaver, G. B. Hoflund, *J. Phys. Chem.* **1994**, *98*, 8519–8524.
[44] S. H. Choi, Y. L. Kim, K. Min Byun, *Opt. Express* **2011**, *19*, 458–466.
[45] V. G. Kravets, A. N. Grigorenko, P. R. Nair, P. Blake, S. Anissimova, K. S. Novoselov, A. K. Geim, *Phys. Rev. B* **2010**, *81*, 155413.
[46] I. Lopez-Salido, D. C. Lim, Y. D. Kim, *Surf. Sci.* **2005**, *588*, 6–18.
[47] P. A. Khomyakov, G. Giovannetti, P. C. Rusu, G. Brocks, J. van den Brink, P. J. Kelly, *Phys. Rev. B* **2009**, *79*, 195425.
[48] D. Yanga, A. Velamakannia, G. Bozoklub, S. Parka, M. Stollera, R. D. Pinera, S. Stankovichc, I. Junga, D. A. Fieldd, C. A. Ventrice Jr., R. S. Ruoff, *Carbon* **2009**, *47*, 145–152.
[49] N. A. Vinogradov, K. Schulte, M. L. Ng, A. Mikkelsen, E. Lundgren, N. Mårtensson, A. B. Preobrajenski, *J. Phys. Chem. C* **2011**, *115*, 9568–9577.
[50] E. Granas, J. Knudsen, U. A. Schroder, T. Gerber, C. Busse, M. A. Arman, K. Schulte, J. N. Andersen, T. Michely, *ACS Nano* **2012**, *6*, 9951–9963.
[51] B. Wang, Y. Puzyrev, S. T. Pantelides, *Carbon* **2011**, *49*, 3983–3988.
[52] S. Malola, H. Häkkinen, P. Koskinen, *Phys. Rev. B* **2010**, *81*, 165447.
[53] P. Y. Huang, C. S. Ruiz-Vargas, A. M. Van der Zande, W. S. Whitney, M. P. Levendorf, J. W. Kevek, S. Garg, J. S. Alden, C. J. Hustedt, Y. Zhu, J. Park, P. L. McEven, D. A. Muller, *Nature*, **2011**, *469*, 389–393.
[54] X. Qi, X. Guo, C. Zheng, *Appl. Surf. Sci.* **2012**, *259*, 195–200.
[55] a) M. Chelvayohan, C. H. B. Mee, *J. Phys. C: Solid State Phys.* **1982**, *15*, 2305; b) A. W. Dweydari, C. H. B. Mee, *Phys. Status Solidi A* **1975**, *27*, 223–230.
[56] P. A. Tipler, R. A. Llewellyyn, *Modern Physics*, 3rd Edition, W. H. Freeman, New York, **1999**.
[57] Y. J. Yu, Y. Zhao, S. Ryu, L. E. Brus, K. S. Kim, P. Kim, *Nano Lett.* **2009**, *9*, 3430–3434.
[58] X. Wang, L. Zhi, K. Mullen, *Nano Lett.* **2008**, *8*, 323–327.
[59] A. Catheline, C. Vallés, C. Drummond, L. Ortolani, V. Morandi, M. Marcaccio, M. Iurlo, F. Paolucci, A. Pénicaud, *Chem. Commun.* **2011**, *47*, 5470–5472.
[60] B. Shan, K. J. Cho, *Phys. Rev. Lett.* **2005**, *94*, 236602.
[61] P. M. Wood, *Biochem. J.* **1988**, *253*, 287–289.
[62] R. Pasricha, S. Gupta, A. K. Srivastava, *Small* **2009**, *5*, 2253–2259.
[63] B. S. Kong, J. Geng, H. T. Jung, *Chem. Commun.* **2009**, 2174.

[64] Z. Yin, S. Wu, X. Zhou, X. Huang, Q. Zhang, F. Boey, H. Zhang, *Small* **2010**, *6*, 307–312.
[65] S.-S. Li, K. H. Tu, C. C. Lin, C. W. Chen, M. Chhowalla, *ACS Nano* **2010**, *4*, 3169–3174.
[66] T. Szabo, O. Berkesi, P. Forgo, K. Josepovits, Y. Sanakis, D. Petridis, I. Dekany, *Chem. Mater.* **2006**, *18*, 2740–2749.
[67] D. Lee, H. Lee, Y. Ahn, Y. Jeong, D. Y. Lee, Y. Lee, *Nanoscale* **2013**, *5*, 7750–7755.
[68] Y. Ahn, Y. Jeong, Y. Lee, *ACS Appl. Mater. Interfaces* **2012**, *4*, 6410–6414.
[69] R. Sachan, V. Ramos, A. Malasi, S. Yadavali, B. Bartley, H. Garcia, G. Duscher, R. Kalyanaraman, *Adv. Mater.* **2013**, 25, 2045–2050.
[70] V. P. Drachev, U. K. Chettiar, A. V. Kildishev, H. K. Yuan, W. Cai, V. M. Shalaev, *Opt. Express* **2008**, *16*, 1186–1195.
[71] M. Losurdo, M.M. Giangregorio, P. Capezzuto, G. Bruno, *J. Phys. Chem. C* **2011**, *115*, 21804–21812.
[72] E. Lodorikis, *J. Quant. Spectrosc. Radiat. Transfer* **2012**, *113*, 2573–2584.
[73] M. G. Moharam, E. B. Grann, D. A. Pommet, T. K. Gaylord, *J. Opt. Soc. Am. A* **1995**, *12*, 1068–1076.
[74] W. Ren, Y. Fang, E. A Wang, *ACS Nano* **2011**, *5*, 6425–6433.
[75] S. W. Joo, Y. S. Kim, *Colloids Surf. A: Physicochem. Eng. Aspects* **2004**, *234*, 117–122.
[76] T. H. Joo, M. S. Kim, K. Kim, **1987**, *18*, 57–60.
[77] J. D. Jackson, in *Classical Electrodynamics*, 3rd. ed, Wiley, New York, **1998**.
[78] Y. R. Shen, *The Principles on Nonlinear Optics*, Wiley, New York **1984**, 141–186.
[79] Q. Hao, B. Wang, J. A. Bossard, B. Kiraly, Y. Zeng, I.-K. Chiang, L. Jensen, D. H. Werner, T. J. Huang, *J. Phys. Chem. C*, **2012**, *116*, 7249–7254.
[80] X. Ling, L. Xie, Y. Fang, H. Xu, H. Zhang, J. Kong, M. S. Dresselhaus, J. Zhang, Z. Liu, *Nano Lett.* **2010**, *10*, 553–561.
[81] W. Xu, J. Xiao, Y. Chen, Y. Chen, X. Ling, J. Zhang, *Adv. Mater.* **2013**, *25*, 928–933.
[82] M. Losurdo, M. M. Giangregorio, G. V. Bianco, P. Capezzuto, G. Bruno, *Thin Solid Films* **2013**, unpublished.
[83] A. C. Ferrari, J. C. Meyer, V. Scardaci, C. Casiraghi, M. Lazzeri, F. Mauri, S. Piscanec, D. Jiang, K. S. Novoselov, S. Roth, A. K. Geim, *Phys. Rev. Lett.* **2006**, *97*, 187401.
[84] S. Howell, D. Kuila, B. Kasibhatla, C. P. Kubiak, D. Janes, R. Reifenberger *Langmuir*, **2002**, *18*, 5120–5125.